


Measurements of low-mode asymmetries in the areal density of laser-direct-drive deuterium–tritium cryogenic implosions on OMEGA using neutron spectroscopy

Cite as: Rev. Sci. Instrum. **93**, 103505 (2022); <https://doi.org/10.1063/5.0101812>

Submitted: 03 June 2022 • Accepted: 17 August 2022 • Published Online: 05 October 2022

 C. J. Forrest, A. Crilly, A. Schwemmlin, et al.





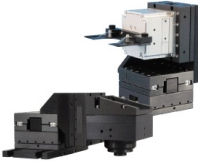
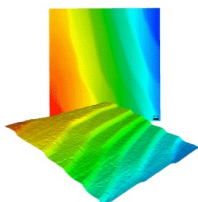
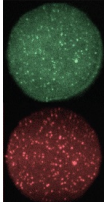
View Online



Export Citation



CrossMark

	<p>Nanopositioning Systems</p> 	<p>Modular Motion Control</p> 	<p>AFM and NSOM Instruments</p> 	<p>Single Molecule Microscopes</p> 
---	--	--	---	--

Measurements of low-mode asymmetries in the areal density of laser-direct-drive deuterium–tritium cryogenic implosions on OMEGA using neutron spectroscopy

Cite as: Rev. Sci. Instrum. 93, 103505 (2022); doi: 10.1063/5.0101812

Submitted: 3 June 2022 • Accepted: 17 August 2022 •

Published Online: 5 October 2022



View Online



Export Citation



CrossMark

C. J. Forrest,^{1,a)} A. Crilly,² A. Schwemlein,¹ M. Gatu-Johnson,³ O. M. Mannion,⁴ B. Appelbe,² R. Betti,¹ V. Yu. Glebov,¹ V. Gopalaswamy,¹ J. P. Knauer,¹ Z. L. Mohamed,¹ P. B. Radha,¹ S. P. Regan,¹ C. Stoeckl,¹ and W. Theobald¹

AFFILIATIONS

¹Laboratory for Laser Energetics, University of Rochester, Rochester, New York 14623-1299, USA

²Centre for Inertial Fusion Studies, The Blackett Laboratory, Imperial College, South Kensington Campus, London, United Kingdom

³Plasma Science and Fusion Center, Massachusetts Institute of Technology, Cambridge, Massachusetts 02139, USA

⁴Sandia National Laboratories, Albuquerque, New Mexico 87185, USA

^{a)}Author to whom correspondence should be addressed: cforrest@lle.rochester.edu

ABSTRACT

Areal density is one of the key parameters that determines the confinement time in inertial confinement fusion experiments, and low-mode asymmetries in the compressed fuel are detrimental to the implosion performance. The energy spectra from the scattering of the primary deuterium–tritium (DT) neutrons off the compressed cold fuel assembly are used to investigate low-mode nonuniformities in direct-drive cryogenic DT implosions at the Omega Laser Facility. For spherically symmetric implosions, the shape of the energy spectrum is primarily determined by the elastic and inelastic scattering cross sections for both neutron–deuterium and neutron–tritium kinematic interactions. Two highly collimated lines of sight, which are positioned at nearly orthogonal locations around the OMEGA target chamber, record the neutron time-of-flight signal in the current mode. An evolutionary algorithm is being used to extract a model-independent energy spectrum of the scattered neutrons from the experimental neutron time-of-flight data and is used to infer the modal spatial variations ($l = 1$) in the areal density. Experimental observations of the low-mode variations of the cold-fuel assembly ($\rho L_0 + \rho L_1$) show good agreement with a recently developed model, indicating a departure from the spherical symmetry of the compressed DT fuel assembly. Another key signature that has been observed in the presence of a low-mode variation is the broadening of the kinematic end-point due to the anisotropy of the dense fuel conditions.

Published under an exclusive license by AIP Publishing. <https://doi.org/10.1063/5.0101812>

I. INTRODUCTION

The OMEGA laser¹ is used to study direct-drive inertial confinement fusion (ICF) by symmetrically irradiating a thin shell target with nominally identical laser beams. The shell is comprised of an outer plastic ablator ($<10 \mu\text{m}$) and a layer of cryogenic deuterium–tritium (DT) ice ($\sim 50 \mu\text{m}$) encapsulating a vapor region of DT gas. In these target designs, the incident laser ablates the thin shell, which then launches one or multiple shocks through

the remaining converging shell and into the vapor region. The shock-transit stage of the implosion is followed by a deceleration phase, where the kinetic energy of the converging shell is converted to the internal energy of the hot spot.² At peak compression, the temperature and density are sufficient to initiate thermonuclear fusion reactions in the DT fuel, resulting in 14.03 MeV neutrons and 3.5 MeV alpha particles.³ To achieve conditions relevant for ignition implosion designs, the hot-spot size must exceed the mean free path of the fusing ions and alpha particles in order to remain

confined in the dense plasma. This requirement is essential to maximize the energy deposition of the alpha particle in the hot spot and surrounding dense fuel. Targets that are not compressed symmetrically will be unable to fully convert their shell kinetic energy to hot-spot thermal energy, reducing the overall fusion yield generated from the implosion.

Nuclear diagnostics are essential to interpreting the condition of the DT plasma during the compression phase in ICF experiments.^{4,5} Measurable parameters that determine the performance of ICF implosions include the ion temperature (T_i), the areal density (ρL), the primary DT neutron yield (Y_n), and the flow velocity of the fusing hot-spot (Ref. 6). Furthermore, the measured broad energy spectrum from the scattering of the primary neutrons off the compressed fuel can be used to investigate low-mode nonuniformities in cryogenic DT implosions. The shape of the neutron energy spectrum is fully determined by the elastic and inelastic scattering cross sections as compared to spherically symmetric target shell conditions.⁷ Deviations from a symmetric implosion are expected to lead to a decrease in target performance metrics, including the yield and 4π average areal density.

In this paper, we describe the two highly collimated neutron time-of-flight detectors that exist on OMEGA and the technique that has been developed to extract a model-independent energy spectrum. Using the resulting neutron energy spectrum from both lines of sight, a reconstruction technique has been developed to produce a 3-D map of the compressed fuel near peak compression and provides a more complete understanding of the symmetry of laser-direct-drive implosions. In the kinematic limit, DT fusion neutrons that undergo direct elastic backscatter from ions lose the largest fraction of their energy possible for a single scattering event. This scattering event produces a sharp edge in the neutron energy spectrum at the kinematic endpoint for both neutron-deuterium (nD) and neutron-tritium (nT). For stationary target ions, the resultant edge energy is dependent only on the ion mass and incoming neutron energy. For nonstationary target ions, it will be shown that the spectral shape of the kinematic end-points is dependent on the scattering rate-weighted ion velocity distribution and variation in the areal density.⁸ These techniques will be demonstrated using data from an experiment with a large mode-1 drive asymmetry. Finally, we discuss the optimal lines of sight with an additional neutron spectrometer that would be required on OMEGA in order to greatly reduce the uncertainties in the 3-D interpretation of the compressed fuel assembly.

II. DISTRIBUTION OF NEUTRONS GENERATED IN A COMPRESSED TARGET

The primary neutron distribution generated once an ICF implosion has reached temperatures and densities sufficient to produce thermonuclear reactions consists of deuterium-deuterium (DD), tritium-tritium (TT), and deuterium-tritium (DT) fusing ions and can be expressed by

$$\frac{dN}{dE} = Y_n \left[\left(\text{DT} + \frac{1}{2} \frac{f_d}{f_t} \frac{\langle \sigma_{v_{dd}} \rangle}{\langle \sigma_{v_{dt}} \rangle} \text{DD} + \frac{f_t}{f_d} \frac{\langle \sigma_{v_{tt}} \rangle}{\langle \sigma_{v_{dt}} \rangle} \text{TT} \right) \right], \quad (1)$$

where Y_n is the primary DT yield, f_d and f_t are the fuel fraction of the fuel, and $\langle \sigma v \rangle$ is the reactivity rate with the associated fusing

pair of ions. In the above expression, DT, DD, and TT represent the shape of the primary neutron energy spectra for each reaction. Once the primary reactions take place, a small fraction of the neutrons produced will scatter throughout the $\sim 30 \mu\text{m}$ hot-spot radius and the $\sim 10 \mu\text{m}$ -thick dense fuel region. These secondary reactions include both the elastic and inelastic scattering contributions that account for $<5\%$ of the total signal. The contributions from the secondary reactions are defined by

$$\frac{dN}{dE} = Y_n \left[\rho L N_A \frac{\sigma_{nd} f_d + \sigma_{nt} f_t + \sigma_{D(n,2n)_p} f_d + \sigma_{T(n,2n)_D} f_t}{f_d m_d + f_t m_t} \right], \quad (2)$$

where ρL is the areal density given as the path integral of mass density from the scattering origin to the spectrometer, N_A is the Avogadro constant, m_d is the mass of the deuteron, m_t is the mass of the triton, and σ is the differential ($d\sigma/dE$) and double-differential ($d^2\sigma/d\Omega dE$) cross section of the different scattering events. The total energy spectrum includes both the primary and secondary contributions and is expressed as

$$\frac{dN}{dE} = \frac{dN}{dE}(\text{primary}) + \frac{dN}{dE}(\text{secondary}). \quad (3)$$

This resultant energy spectrum (dN/dE) in Eq. (3) does not include any asymmetric fuel contribution in the second term. In experiments, several factors can introduce perturbations, including target offset, ice-layer nonuniformity, and laser-beam energy imbalance, which have been shown to result in variations of the dense fuel. Information about the asymmetry of the dense region is embedded in the energy spectrum. The elastic interactions are a direct mapping between scattering angle and outgoing neutron energy. This results in the number of scattered neutrons in a particular neutron energy range containing information on the areal density along a specific neutron-scattering angle and therefore a specific region of the dense fuel.

The differential and double-differential cross-sections require a $\cos \theta$ term to better describe this variation in the cold fuel, assuming a low-mode ($l = 1$) distribution as given by

$$\frac{d\sigma}{dE} = \int \left(\frac{d\Omega}{dE} \frac{d\sigma}{d\Omega} \right) \left(1 + \frac{\Delta\rho L}{\rho L} \times \cos \theta \right) dE, \quad (4)$$

$$\frac{d\sigma_{n,2n}}{dE} = \int 2\pi \frac{d^2\sigma}{dE d\Omega} \left(1 + \frac{\Delta\rho L}{\rho L} \times \cos \theta \right) \times d\cos \theta. \quad (5)$$

Here, the addition of the $\Delta\rho L/\rho L$ allows for the shape of the energy spectrum below the primary DT signal to follow a mode-1 distribution. With the current areal densities achieved on OMEGA, the single-scatter approximation limits the scope of this model to $<200 \text{ mg/cm}^2$. At higher areal densities, multiple scattering becomes increasingly important, with the approximations required leading to a more invalid model.⁷ In practice, a high-dynamic-range spectrometer is required to observe this neutron signal several orders of magnitude below the primary DT reaction.⁹

III. HIGH-DYNAMIC-RANGE NEUTRON TIME-OF-FLIGHT SPECTROMETERS

To measure neutron spectra over a dynamic range of 10^6 while maintaining sensitivity in the instrument, several difficulties must be considered. For example, the dominant primary DT peak accounts for more than 90% of the neutron energy deposited in the spectrometer. Such a large impulse incident on the spectrometer will produce a long-light afterglow component in the scintillator. This causes the lower-energy neutrons in the detector to be masked by the afterglow component from the primary peak that is still present from the scintillation process. Another consideration for high-yield DT implosions is the neutron scattering from the target chamber walls and surrounding concrete structures. One method employed to achieve a high signal-to-background with minimal light afterglow was a double-collimated line of sight with a low-light afterglow scintillator.¹⁰ Ultrafast gating microchannel-plate photomultiplier tubes (MCP-PMTs) were implemented to gate out the primary DT peak to measure the low-energy neutron spectrum.

To meet these requirements, spectrometers were designed to utilize an advanced scintillator compound with low-afterglow characteristics used to minimize the masking of additional neutron components after the dominant primary DT peak. The diagnostic consists of a 2 mm-thick stainless-steel cylindrical housing that is 20 cm in diameter and 10 cm deep, which contains the scintillation fluid. Thin (<0.5 cm) stainless-steel plates are used to seal the cylindrical housing to minimize neutron attenuation normal to the line of sight. In this study, two identical neutron spectrometers each with four-MCP-PMTs are positioned at a distance of 13.4 and 22.1 m from the target chamber center on the OMEGA Laser System, as shown in Fig. 1.

Scintillation light from the incident neutrons is viewed through fused-silica windows, where the light is coupled to four 40 mm-diam PMTs.⁵ The instrument needs to be positioned close enough to achieve high-neutron statistics but far enough away to interpret the individual components of the energy spectrum. The signals from

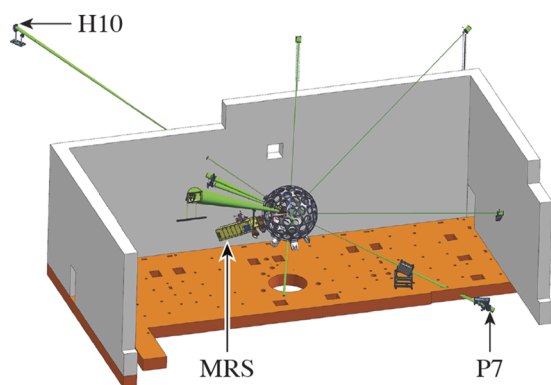


FIG. 1. Two neutron spectrometers have highly collimated lines of sight on OMEGA along the P7 and H10 ports located outside the target bay concrete shielding. The blue structure is the target chamber, and the green lines are projected to the neutron time-of-flight spectrometers at distances of 13.4 and 22.1 m, respectively. The magnetic recoil spectrometer (MRS) that measures the scattered neutrons using a knock-on deuteron technique is mounted directly in the target chamber.

the PMTs are recorded by a 1 GHz Tektronix® DPO-7104 digital oscilloscope. A 3-D drawing of the spectrometers used along the P7 and H10 lines of sight is shown in Fig. 2.

These spectrometers have the unique ability to measure the primary neutron energy spectrum and the down-scattered portion of the neutron energy spectrum (1–15 MeV). Due to detector resolution constraints, the forward-scattered region (8–12 MeV) is not fully resolved and is not discussed in this present analysis. The areal density is currently inferred by measuring the number of scattered neutrons in the 3–8 MeV region, which corresponds to neutrons with an average scattering cosine of $\mu = -0.75$ –0.50. Therefore, the neutron time-of-flight (nTOF) spectrometers infer the areal density in the region of the target along the opposing (backscattered region) detectors' lines of sight. An alternative approach used to measure the scattered neutrons relies on a knock-on deuteron technique.

A magnetic recoil spectrometer (MRS) is mounted directly on the OMEGA target chamber, and it uses neutrons from the fusing ions that elastically scatter off of a CD_2 conversion foil, which is placed a specific distance from the implosion, resulting in the production of recoiled deuterons. The recoiled deuterons exit forward and are directed through the aperture of the magnet, which is spatially dispersed as they propagate through the magnetic field due to their different velocities. An array CR-39 coupon is positioned to record the incident deuterons as a function of the deflection angle that is directly related to the recoil energy.¹¹

The present configuration of the MRS detector on OMEGA measures the primary DT neutron energy spectrum and the forward-scattered portion of the neutron energy spectrum (9–11 MeV). Due to detector resolution limitations, only the primary DT fusion yield is currently able to be accurately inferred from the primary DT spectrum. In this approach, the areal density is inferred by measuring the number of primary DT neutrons as compared to the signal in the 9–11 MeV region of the scattered

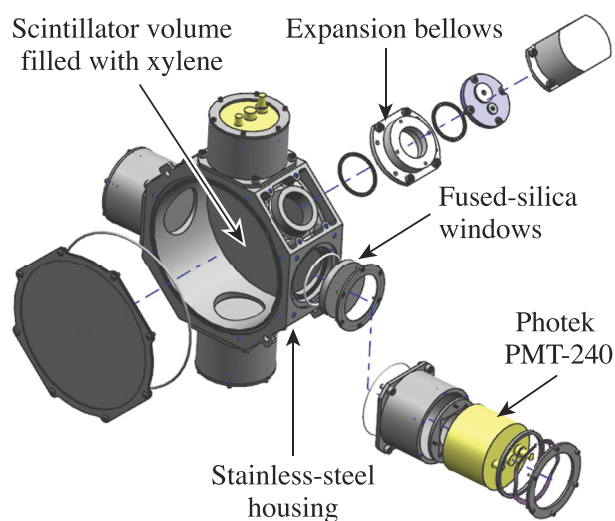


FIG. 2. A CAD drawing of the neutron time-of-flight (nTOF) detector shows a cavity for the scintillation fluid, the fused-silica windows, and the photomultiplier tube (PMT) mounts.

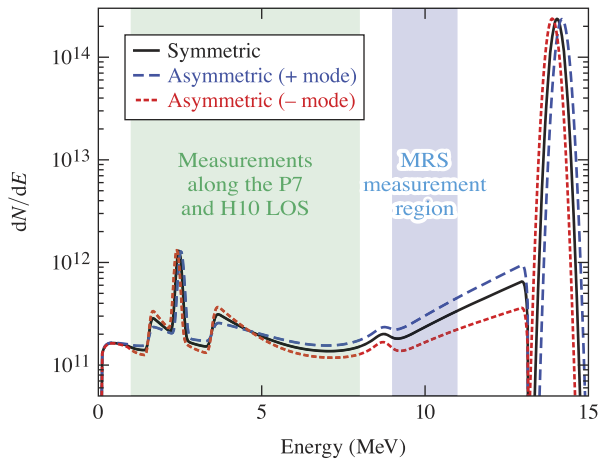


FIG. 3. The two highly collimated lines of sight (P7 and H10) measure the neutrons that scatter off the backside of the target in the energy region from 1 to 8 MeV, shown in two spherical sections (shaded in green). A third diagnostic (MRS) measures the energy spectrum in a 9–11 MeV band (shaded in blue). Examples of low mode asymmetries for both a positive mode (blue dashed) and a negative mode (red dashed) $l = 1$ that would be present in the energy spectrum as viewed by the spectrometer are shown.

neutron spectrum that corresponds to neutrons with an average scattering cosine of $\mu = 0.4$ – 0.7 . A computer model of the MRS detector mounted on the target chamber is shown in Fig. 1. With the two highly collimated nTOF's and the MRS, a large fraction of the scattered neutrons from a compressed target are observed. A representation of the spectral coverage for each spectrometer is shown in Fig. 3.

An additional effect observed in the energy distribution is a mean energy shift of the primary DT and DD peak distributions. The shift in the primary peak is due to the hot-spot flow, which has been shown to have a strong correlation in the direction of the minimum areal density. The main advantage of evaluating the spectrum over an extended region is to interrogate the scattered neutrons for variations in the dense fuel assembly. An example neutron spectrum for a modal variation in the areal density that would be expected in the energy spectrum from the scattered neutrons is shown in Fig. 3 with a positive and negative mode $l = 1$. Presently, the current experimental setup cannot resolve higher spatial modes ($l > 2$) in the resultant energy spectrum.

Over the extended energy region, this model illustrates the motivation for using the scattered neutron energy spectrum to understand the effects of areal-density asymmetries. However, due to the limited energy region, it would be challenging for the current MRS to extract variations in the energy spectrum because of modal perturbations in the ~ 10 MeV energy region.

IV. MODEL-INDEPENDENT ENERGY SPECTRUM

The nTOF on OMEGA operates in current mode and measures the neutron flux incident on the detector. The time record is directly related to the energy of the emitted neutron based on the known distance of the detector to the source. Traditional forward-fitting requires a detector model for the data and may thereby

introduce undesired biases to the analysis.¹² The new concept presented here begins with a user-defined minimum number of node points to construct a continuous-energy spectrum by interpolation. The neutron yield at each node is changed randomly, where only changes producing a better match to the data are accepted. After a certain number of iterations, additional nodes are added at random energies, where again, only favorable choices are accepted. This technique is commonly referred to as a genetic or evolutionary algorithm.

A. Evolutionary algorithm

A distinct advantage of this evolutionary algorithm (EA) is the ability to include all of the known quantities of the experimental setup and detection system (nTOF). The effects of the instruments on the measured neutron energy spectrum dN/dE can be expressed by

$$I(t) = \left[\varepsilon_{\text{scint}}(E) \varepsilon_{\text{los}}(E) \frac{dN}{dE} \frac{dE}{dt} \right] \otimes R(E, t), \quad (6)$$

where $\varepsilon_{\text{scint}}(E)$ is the light sensitivity of the scintillator, $\varepsilon_{\text{los}}(E)$ is the neutron attenuation along the associate line of sight, dE/dt is the Jacobian, and $R(E, t)$ is the response function of the detection system.¹³ The light sensitivity and line of sight attenuation were modeled using a neutron transport code.

The EA forward fits the desired neutron spectrum dN/dE according to Eq. (6) to produce a hypothetical nTOF spectrum $I(t)$ that is compared to the experimental signal. The full iterative approach is summarized by

$$\frac{dN_1}{dE} \rightarrow \sum \frac{[I(t)_{\text{signal}} - I(t)_1]^2}{I(t)_1} = \chi_1^2, \quad (7)$$

$$\frac{dN_2}{dE} \rightarrow \sum \frac{[I(t)_{\text{signal}} - I(t)_2]^2}{I(t)_2} = \chi_2^2, \quad (8)$$

whenever

$$\chi_1^2 < \chi_2^2 \rightarrow \frac{dN_1}{dE}, \quad (9)$$

i.e., return to the old solution. Otherwise,

$$\chi_1^2 > \chi_2^2 \rightarrow \frac{dN_3}{dE} \quad (10)$$

accepts the new solution. The procedure is repeated until χ^2 over the complete time spectrum reaches a plateau, which is automatically detected. Several adjustments have been made and tested to this basic elementary evolutionary algorithm to prevent overfitting, which was also described in a similar algorithm.¹⁴ It was found that a very effective way to limit overfitting is nested fitting. The fit starts with a small number of nodes, to which more nodes are added one at a time. For each fit, the χ^2 value is allowed to reach a plateau, after which another point is included at a random energy and the fitting procedure is repeated. Using parallel computing, several spectra with different node points are fitted simultaneously, and the fit with the smallest χ^2 is the basis for including the next point.

B. Monte Carlo simulations

The fitting routine requires the detector light sensitivity and the line-of-sight attenuation for the specified spectrometer along the P7 and H10 locations. These detector effects are modeled using a neutron transport code, namely, Monte Carlo N-Particle (MCNP). The simulations show that the primary DT neutron detectors on OMEGA, the detector sensitivity, and line of sight attenuation do not vary significantly across the narrow (<1 MeV) range of neutron energies analyzed by these detectors, as shown in Fig. 3. For the primary DD and scattered-neutron detectors, the MCNP calculations reveal that the detector sensitivity can vary 10%–20% below 4 MeV, while the line-of-sight attenuation can vary ~5% across the energy ranges that are analyzed. Therefore, in the analysis of the raw time-of-flight spectra, the exact shape of the detector sensitivity and line of sight attenuation are included.¹²

V. DATA ANALYSIS

The two lines of sight from each spectrometer have an inherent background that is due to the residual neutron scattering from the environment, such as the target chamber, surrounding steel, and concrete structures necessary to hold the mirror assemblies. An approach to inferring this background contribution is dedicated experiments, evaluating the shape of the scattered neutrons with implosions that have minimal areal density. In this study, we looked at thin CH shells and exploding pushers with apparent temperatures below 6 keV to mitigate any kinetic effect that leads to yield ratio anomalies and inaccurate distributions of the primary reactions.

A. Three-dimensional reconstruction

Once the background has been accounted for the remaining model-independent energy spectrum is used to extract key implosion metrics. A fit to the data uses Eq. (3) with the modal variation addition in Eqs. (4) and (5) to provide an areal density ρL_0 and variation ρL_1 for the P7 and H10 lines of sight,

$$\rho L_{\text{los}}(\Omega) = \rho L_0 + \rho L_1 \Omega \cdot \hat{\mu}_{\text{hs}},$$

where

$$\rho L_1 = \frac{\Delta \rho L \times \rho L_0}{\Omega_{\text{det}} \cdot \hat{\mu}_{\text{hs}}},$$

with the required inputs such as the primary DT yield, apparent ion temperature, and fuel fraction used to fill the targets. Preliminary fits (not shown) indicated that the region between the DD peak (2.45 MeV) and the nT kinematic end point (3.52 MeV) underestimated the experimental data are believed to be due to the contribution from the triton breakup that was not initially included in the analysis.

Earlier experimental energy spectra of protons and deuterons produced in accelerator experiments from the triton breakup reactions, T(n, 2n)D and T(n, 3n)p, were barely significant (deuterons) and not significant (protons) given the experimental uncertainties, respectively.¹⁵ It is unknown if other experimental data for these reactions has been published. The shape of the energy spectrum for the double differential cross section was calculated using the

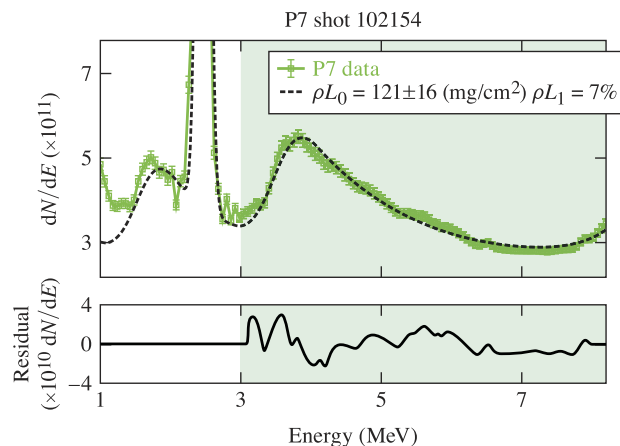


FIG. 4. A fit to the experimental data with the statistical uncertainty and the model (dashed black line) in the energy region from 3 to 8 MeV along the P7 line of sight. Below the D_2 peak at 2.45 MeV, the nD kinematic endpoint is observed.

Evaluated Nuclear Data File (ENDF) LAW = 6. The cross section for this reaction has been calculated to be 19 mb (Ref. 16).

An example of a fit to the experimental data from an experimental campaign in October of 2021 is shown in Figs. 4 and 5 for the P7 and H10 locations.

The energy region from 1 to 8 MeV is resolved in the P7 location. However, the region below the DD peak along the H10 line of sight is not well resolved due to a larger background contribution. At the present time, the fit region is being evaluated from 3 to 8 MeV. Below the D_2 peak, we need to consider the scattering of DD primary neutrons and multi-scatters of DT neutrons that become more significant. Additionally, the spectral shapes of the TT primaries and inelastic break up reactions are more

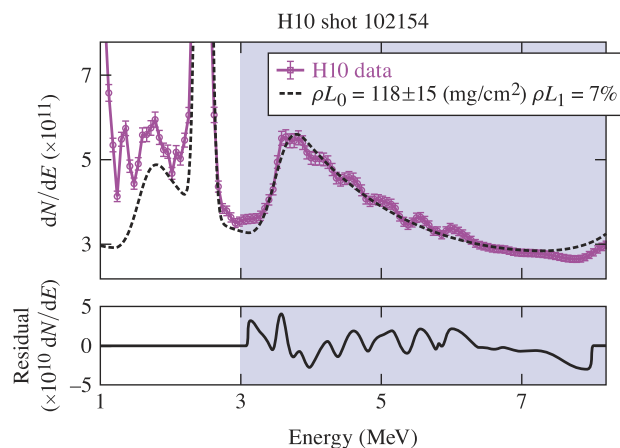


FIG. 5. A fit to the experimental data (purple) with the statistical uncertainty and the model (dashed black line) in the energy region from 3 to 8 MeV along the H10 line of sight. In this spectrometer, the region below the D_2 peak is mostly unresolved, and the nD kinematic end point is less evident when compared to the P7 line of sight (see Fig. 4).

TABLE I. Experimental values from October 2021.

Shot no.	ρL_0 (P7) (mg/cm ²)	ρL_1	ρL_0 (H10) (mg/cm ²)	ρL_1	v_{hs} (km/s)
102 145	105 ± 12	0.01	101 ± 11	0.32	45
102 149	98 ± 11	0.03	95 ± 11	0.26	51
102 154	118 ± 13	0.03	111 ± 13	0.09	66
102 158	107 ± 12	0.12	105 ± 12	0.10	75
102 162	116 ± 13	0.24	112 ± 13	0.09	100

uncertain at lower energies. During the October 2021 campaign, there were five experiments with the experimental values listed in Table I.

The best performer in this campaign was shot 102 154, which had a $Y_n = 2.22 \times 10^{14}$ and the highest ρL and the lowest variation along both lines of sight. The worst performer of the day was shot 102 162 that had an $Y_n = 1.79 \times 10^{14}$ and a significant hot-spot flow and an observed low mode. To better understand how the variation in the areal density impacts implosion performance, an accurate reconstruction of the areal-density distribution over 4π is required.

To reconstruct the areal density using the inferred values, ($\rho L_0 + \rho L_1$) several radiation-hydrodynamic simulations, along with recent experiments on OMEGA, have shown that there are strong correlations between the direction of the measured hot-spot velocity and the areal-density asymmetry direction.¹⁷ It is expected that the direction of minimum areal density is expected to be along the direction of the hot-spot velocity. As a result, a mode $l = 1$ areal-density distribution and the direction of the hot-spot flow is expressed by

$$\rho L(\Omega) = \overline{\rho L_0} + \overline{\rho L_1} \Omega \cdot \mu_{hs}, \quad (11)$$

where $\overline{\rho L_0}$ and $\overline{\rho L_1}$ are the mean values of the areal density and variation in the areal density projected along the hot-spot flow velocity μ_{hs}

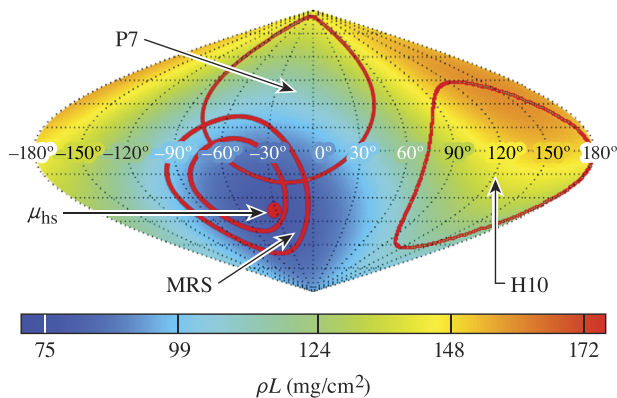


FIG. 6. A reconstruction of the areal density using the P7 and H10 neutron spectrometers. Due to the limited number of spectrometers, the minimum areal density is constrained to be directed along the direction of the hot-spot flow vector μ_{hs} noted by the red dot.

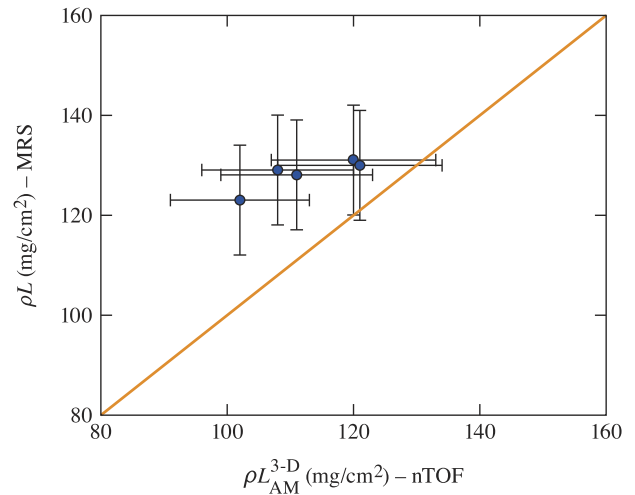


FIG. 7. The arithmetic mean from the 3-D reconstruction is compared to the areal density inferred from the MRS spectrometer.

is measured by independent detectors.¹⁸ An example of the reconstruction of the areal density from the implosions with a significant mode 1 is shown in Fig. 6. With the minimum areal density directed just below the P7 axis, there is up to a factor of 2 in the variation of the dense fuel.

To further constrain the inferred areal density, a comparison between the MRS and the nTOF is shown in Fig. 7. In this comparison, the arithmetic mean from the nTOF measurements is calculated by integrating the overall reconstructed areal-density values given by

$$\rho L_{am} = \frac{1}{4\pi} \int \rho L \, d\cos\theta \, d\phi. \quad (12)$$

To achieve this reconstruction without an assumption on the direction of the low mode (i.e., $l = 1$), up to four spectrometers are required to measure the scattered neutron spectra. Therefore, with four strategically located and highly collimated lines of sight, a reconstruction of the areal-density distribution over 4π can be inferred without an assumption on the direction of the low mode.¹⁹ The optimal lines of sight required with the currently installed spectrometers on OMEGA to achieve a full reconstruction are given in Table II.

TABLE II. Current and future lines of sight for the optimal 3-D reconstruction of the dense fuel.

LOS	Distance (m)	θ (deg)	ϕ (deg)
P7	13.4	116.5	162
H10	22.1	79.2	306
LOS 3	N/A	150	225
LOS 4	N/A	70	100

These positions of the four neutron spectrometers represent a tetrahedron configuration and would provide the required coverage to better resolve asymmetries below 10% of the compressed fuel when evaluating the energy region from 3 to 8 MeV.

It is believed that low-mode asymmetry in a directly driven ICF implosion is a limiting factor for performance. A recent model demonstrates that an asymmetric-piston description can be used to show the impact of mode-1 shell asymmetry and degradation in performance.¹⁷ In this model, the increase in areal-density variation is correlated with yield degradation and is expressed by

$$\frac{Y}{Y_{LLAC}} = (1 - f^2)^a, \quad (13)$$

where a is given to be 3.3, and f is the variation in the areal density and is expressed by

$$f = \frac{\rho L_{\max} - \rho L_{\min}}{\rho L_{\max} + \rho L_{\min}} \quad (14)$$

with ρL_{\max} and ρL_{\min} obtained from the 3-D reconstruction technique. As with the increase in the variation in the areal density, a correlation with yield degradation is observed, but more data are required to assess if the trend is consistent with the piston model. However, the variation in the areal density compared to the measured yield and divided by the 1D LILAC yield is up to 40% lower, as shown in Fig. 8 with the solid black line. This can be explained by other mechanisms that degrade the yield that is not associated with low-mode variation in the areal density.

B. Hydrodynamic properties from kinematic edges

Recent theoretical⁸ and experimental²⁰ studies have shown that the neutron-backscatter edge presents a novel measurement of the

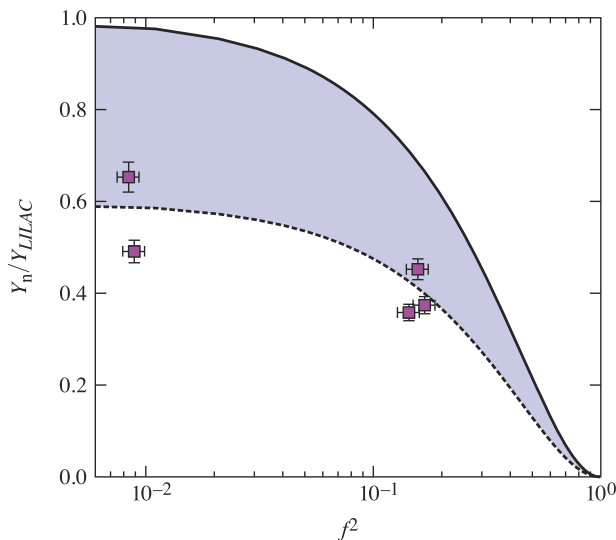


FIG. 8. The increase in areal-density variation from the experimental campaign is beginning to show a correlation with yield degradation. A reduction in overall performance of ~40% (shaded region) is likely caused by other degradation mechanisms due to higher modes, such as laser imprint, mid-modes from beam mode, etc.

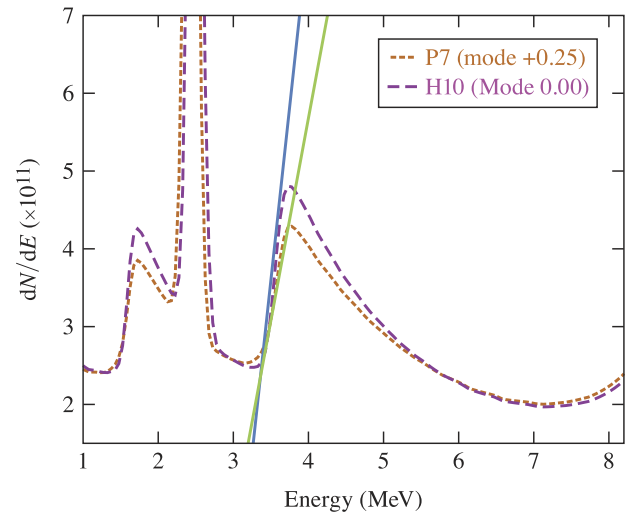


FIG. 9. A model illustrates the broadening of the kinematic edge due to the anisotropy of the cold fuel depending on the spectrometers' line of sight. Straight lines tangent to the nT edges are included to emphasize the difference in slopes.

hydrodynamic conditions at stagnation. The spectral shape of the edge is determined by the velocity distribution of the scattering ions.⁸ When there is a large mode-1 variation in areal density, hydrodynamic models predict that the higher areal density side will decelerate slower than the lower areal density side.²¹ Therefore, the lower areal density side will exhibit a larger variation in scattering ion velocities and will produce a broader backscatter edge; the opposite is true for the higher areal density side. This anisotropy has been predicted in simulation to appear in the

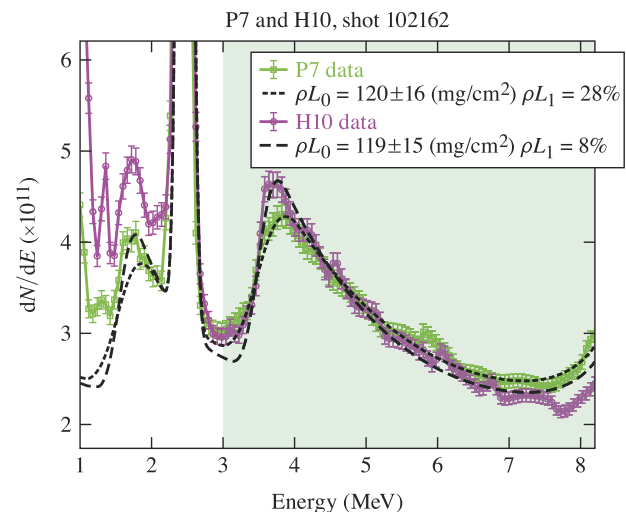


FIG. 10. An example of a cryogenic implosion with a significant mode 1 that shows qualitative agreement with the broadening of the kinematic edge due to the anisotropy of the cold fuel depending on the spectrometers' line of sight as predicted by the model.

backscatter edge shape along different lines of sight.²² More recent hydrodynamics simulations of OMEGA implosions perturbed by a mode 1 were post-processed with a neutron transport code to obtain synthetic spectra on the P7 and H10 OMEGA lines of sight showing the anisotropic edge broadening. The results are shown in Fig. 9.

Measurements on the broadening of the kinematic edges (Fig. 10) show qualitative agreement with the anisotropy of the dense fuel conditions from separate lines of sight given by the model prediction (Fig. 9). The anisotropy is also correlated with the observed mode-1 areal-density asymmetry.

The P7 line of sight observes a positive mode-1 areal-density asymmetry and, therefore, backscatter is occurring in a lower areal density region for this line of sight.

The backscatter edge is broader along P7, which matches our model prediction that the lower areal density side should decelerate more rapidly.

VI. SUMMARY

In this manuscript, a novel data analysis approach was introduced using an evolutionary algorithm to extract a model-independent energy spectrum of the scattered neutrons from the experimental neutron time-of-flight data. This technique allows for a more detailed analysis of the scattered spectra required to infer the modal spatial variations ($l = 1$) in the compressed fuel areal density. Experimental observations of the low-mode variations of the cold fuel assembly ($\rho L_0 + \rho L_1$) show good agreement with a recently developed model, indicating a departure from spherical symmetry in the compressed DT fuel assembly. The contribution of the deuteron and triton breakup in the implosion target is non-negligible and is treated in the inference of the areal density. In one example with a significant mode, with the minimum areal density directed along the hot-spot flow, demonstrates the novel ability to resolve modal variations in the fuel assembly. The addition of two more highly collimated lines of sight is required to reconstruct the areal density in 4π without any assumption on the direction of the low mode.

In addition to the inferred areal-density asymmetry, it was observed that the shape of the nT kinematic edge varied between different lines of sight. This can be explained by anisotropy in dense fuel conditions coincident with the areal-density asymmetry. The observed change in nT edge shape is correlated with the hot-spot velocity and areal density variation direction. This is in line with hydrodynamic model predictions that show differential deceleration of the fuel shell in the presence of a mode-1 asymmetry.

ACKNOWLEDGMENTS

This work was supported by the U.S. Department of Energy Office of Inertial-Confinement Fusion under cooperative Agreement No. DE-NA0003856, the University of Rochester, and the New York State Energy Research and Development Authority. Sandia National Laboratories is a multi-mission laboratory managed and operated by National Technology and Engineering Solutions of Sandia, LLC, a wholly-owned subsidiary of Honeywell International, Inc., for the U.S. Department of Energy's National Nuclear

Security Administration under Contract No. DE-NA0003525. This report was prepared as an account of work sponsored by an agency of the U.S. Government. Neither the U.S. Government nor any agency thereof, nor any of their employees, makes any warranty, express or implied, or assumes any legal liability or responsibility for the accuracy, completeness, or usefulness of any information, apparatus, product, or process disclosed, or represents that its use would not infringe privately owned rights. Reference herein to any specific commercial product, process, or service by trade name, trademark, manufacturer, or otherwise does not necessarily constitute or imply its endorsement, recommendation, or favoring by the U.S. Government or any agency thereof. The views and opinions of authors expressed herein do not necessarily state or reflect those of the U.S. Government or any agency thereof.

AUTHOR DECLARATIONS

Conflict of Interest

The authors have no conflicts to disclose.

Author Contributions

C. J. Forrest: Writing – original draft (lead). **A. Crilly:** Formal analysis (equal). **A. Schwemlein:** Formal analysis (equal). **M. Gatu-Johnson:** Writing – review & editing (equal). **O. M. Mannion:** Writing – review & editing (equal). **B. Appelbe:** Writing – review & editing (equal). **R. Betti:** Writing – review & editing (equal). **V. Yu. Glebov:** Writing – review & editing (equal). **V. Gopalaswamy:** Writing – review & editing (equal). **J. P. Knauer:** Writing – review & editing (equal). **Z. L. Mohamed:** Writing – review & editing (equal). **P. B. Radha:** Writing – review & editing (equal). **S. P. Regan:** Writing – review & editing (equal). **C. Stoeckl:** Writing – review & editing (equal). **W. Theobald:** Writing – review & editing (equal).

DATA AVAILABILITY

The data that support the findings of this study are available from the corresponding author upon reasonable request.

REFERENCES

- ¹T. R. Boehly *et al.*, *Opt. Commun.* **133**, 495 (1997).
- ²J. Nuckolls, L. Wood, A. Thiessen, and G. Zimmerman, *Nature* **239**, 139 (1972).
- ³H. Brysk, *Plasma Phys.* **15**, 611 (1973).
- ⁴V. Y. Glebov, C. Stoeckl, T. C. Sangster, C. Mileham, S. Roberts, and R. A. Lerche, *Rev. Sci. Instrum.* **77**, 10E712 (2006).
- ⁵C. J. Forrest, V. Y. Glebov, V. N. Goncharov, J. P. Knauer, P. B. Radha, S. P. Regan, M. H. Romanofsky, T. C. Sangster, M. J. Shoup, and C. Stoeckl, *Rev. Sci. Instrum.* **87**, 11D814 (2016).
- ⁶O. M. Mannion *et al.*, *Phys. Plasmas* **28**, 042701 (2021).
- ⁷A. J. Crilly, B. D. Appelbe, O. M. Mannion, C. J. Forrest, and J. P. Chittenden, *Phys. Plasmas* **28**, 022710 (2021).
- ⁸A. J. Crilly, B. D. Appelbe, O. M. Mannion, C. J. Forrest, V. Gopalaswamy, C. A. Walsh, and J. P. Chittenden, *Phys. Plasmas* **27**, 012701 (2020).
- ⁹C. J. Forrest *et al.*, *Rev. Sci. Instrum.* **83**, 10D919 (2012).

- ¹⁰R. Lauck, M. Brandis, B. Bromberger, V. Dangendorf, M. B. Goldberg, I. Mor, K. Tittelmeier, and D. Vartsky, *IEEE Trans. Nucl. Sci.* **56**, 989 (2009).
- ¹¹J. A. Frenje *et al.*, *Rev. Sci. Instrum.* **79**, 10E502 (2008).
- ¹²R. Hatarik *et al.*, *J. Appl. Phys.* **118**, 184502 (2015).
- ¹³Z. L. Mohamed *et al.*, *J. Appl. Phys.* **128**, 214501 (2020).
- ¹⁴E. P. Hartouni, B. Beeman, J. A. Caggiano, C. Cerjan, M. J. Eckart, G. P. Grim, R. Hatarik, A. S. Moore, D. H. Munro, T. Phillips, and D. B. Sayre, *Rev. Sci. Instrum.* **87**, 11D841 (2016).
- ¹⁵J. Mailen Kootsey, *Nucl. Phys. A* **113**, 65 (1968).
- ¹⁶A. Deltuva and A. C. Fonseca, *Phys. Rev. C* **86**, 011001(R) (2012).
- ¹⁷O. A. Hurricane, D. T. Casey, O. Landen, D. A. Callahan, R. Bionta, S. Haan, A. L. Kritcher, R. Nora, P. K. Patel, P. T. Springer, and A. Zylstra, *Phys. Plasmas* **29**, 012703 (2022).
- ¹⁸O. M. Mannion, J. P. Knauer, V. Y. Glebov, C. J. Forrest, A. Liu, Z. L. Mohamed, M. H. Romanofsky, T. C. Sangster, C. Stoeckl, and S. P. Regan, *Nucl. Instrum. Methods Phys. Res., Sect. A* **964**, 163774 (2020).
- ¹⁹F. Weilacher, P. B. Radha, and C. Forrest, *Phys. Plasmas* **25**, 042704 (2018).
- ²⁰O. M. Mannion *et al.*, *Phys. Rev. E* **105**, 055205 (2022).
- ²¹B. K. Spears *et al.*, *Phys. Plasmas* **21**, 042702 (2014).
- ²²A. J. Crilly *et al.*, *Phys. Plasmas* **25**, 122703 (2018).